Assessing the Risk of Potential Tsunamigenic Earthquakes in the Mentawai Region by Seismic Imaging, Central Sumatra

Yanfang Qin, Jian Chen, Satish Singh, Nugroho Hananto, Helene Carton, Paul Tapponnier

Geochemistry, Geophysics, Geosystems

RESEARCH ARTICLE
10.1029/2023GC011149

Assessing the Risk of Potential Tsunamigenic Earthquakes in the Mentawai Region by Seismic Imaging, Central Sumatra

Yanfang Qin[1], Jian Chen[1], Satish C. Singh[2], Nugroho Hananto[3], Helene Carton[2], and Paul Tapponnier[4]

[1]Japan Agency for Marine-Earth Science and Technology, Yokohama Institute for Earth Science, Yokohama, Japan, [2]Institut de Physique du Globe de Paris (CNRS—Université Paris Cité), Paris, France, [3]Research Center for Deep Sea, Indonesian Institute of Sciences, Jakarta, Indonesia, [4]Institute of Crustal Dynamics (ICD), China Earthquake Administration (CEA), Beijing, China

Key Points:

- The deformation structures at the wedge front consist of mixed vergent ramp faults and varying stratigraphic levels of décollements
- The mapped deformation structures in the unruptured segment are similar to those observed in the 2010 M_w7.8 tsunami earthquake rupture zone
- The along-strike variations of the basal friction along the megathrust may indicate different coseismic behaviors and tsunami risk

Supporting Information:

Supporting Information may be found in the online version of this article.

Correspondence to:

Y. Qin,
qinyf@jamstec.go.jp

Citation:

Qin, Y., Chen, J., Singh, S. C., Hananto, N., Carton, H., & Tapponnier, P. (2024). Assessing the risk of potential tsunamigenic earthquakes in the Mentawai region by seismic imaging, Central Sumatra. *Geochemistry, Geophysics, Geosystems*, *25*, e2023GC011149. https://doi.org/10.1029/2023GC011149

Received 24 JULY 2023
Accepted 29 MAR 2024

Author Contributions:

Conceptualization: Yanfang Qin, Helene Carton
Data curation: Yanfang Qin, Nugroho Hananto, Helene Carton, Paul Tapponnier
Formal analysis: Yanfang Qin
Investigation: Yanfang Qin
Methodology: Yanfang Qin, Jian Chen
Software: Yanfang Qin
Validation: Yanfang Qin
Visualization: Yanfang Qin
Writing – original draft: Yanfang Qin, Jian Chen

Abstract In the marginal regions along subduction zones, oceanic plates subducting beneath continental plates produce the largest number of earthquakes on Earth and sometimes devastating tsunamis. The lateral segmentation of earthquakes along the Sumatra subduction zone is well documented. However, the entirely different seismic behaviors among the segments indicate that local structures are key elements controlling coseismic slip propagation; in particular, frontal accretionary prism structures are closely associated with tsunami generation. Offshore of Central Sumatra, in the Mentawai segment, large earthquakes nucleated in 2007 and 2010 caused many human casualties and a great deal of property loss. Using seismic reflection data, we show the subsurface structure of accretionary over a significant portion of the frontal wedge that did not rupture during the 2007 earthquake, and this area remains locked. The subsurface deformation structure at the wedge front, which is similar to that in the 2010 M_w7.8 tsunami earthquake rupture zone, suggests the potential for a large tsunami earthquake in the near future. On the other hand, the along-strike variations of the effective basal friction at shallow depth may indicate that different coseismic behaviors are caused by a sudden failure of the deeper seismogenic zone.

Plain Language Summary In certain areas where oceanic plates slide beneath continental plates (subduction zones), earthquakes and tsunamis, such as those seen in the Sumatra region, can lead to significant loss. Although previous studies show that earthquakes are segmented along the Sumatra subduction zone, indicating distinct seismic behaviors, the reasons behind these differences are not well understood. This study focuses on the Mentawai segment off Central Sumatra, where large earthquakes occurred in 2007 and 2010, causing casualties and property damage. We use seismic reflection data to image the subsurface structure of the frontal wedge, an area associated with tsunami generation. In the portion of the wedge that did not rupture during the 2007 earthquake, our results indicate a potential threat of a future large tsunami earthquake. Interestingly, the different earthquake behaviors might be explained by variations in basal friction along the plate boundary fault. This research enhances our understanding of the factors influencing earthquake and tsunami generation in subduction zones, with implications for future hazard assessments.

1. Introduction

The active Sumatra subduction zone, where the Indo-Australian plate is subducting beneath the Sunda plate, has hosted many large devastating tsunamigenic earthquakes in recent decades. In addition to the 2004 M_w 9.1 Sumatra–Andaman earthquake and the 2005 M_w 8.6 Nias earthquake in northern Sumatra (e.g., Borrero et al., 2011; Lay et al., 2005), the 1994 M_w 7.8 Liwa earthquake occurred in southern Sumatra (Widiwijayanti et al., 1996), and the 2007 M_w 8.4 and 2010 M_w 7.8 Mentawai earthquakes occurred in central Sumatra (Konca et al., 2008; Newman et al., 2011). Among these events, the 2010 Mentawai earthquake nucleated offshore of South Pagai island (Figure 1), and generated a large tsunami with a run-up of up to 16 m along ~100 km of coastline that inundated areas more than 300 m inland. In 2007, an M_w 8.4 earthquake occurred ~200 km SE of the epicenter of the 2010 event that generated a large slip (~10 m) in a patch 100 km long and 50 km wide ~100 km northwest of the epicenter (Figure 1) but shallow slip of only 2–3 m near the hypocenter. This rupture seems to have initiated at 20–30 km depth, but the slip release was small or absent at shallow depths (10–15 km) (Lorito et al., 2008). Another earthquake with M_w 7.9 with the hypocenter at 43 km depth occurred 12 hr after and ~200 km north of the epicenter of the M_w 8.4 event (Borrero et al., 2009), and the next day, an M_w 7.0 event

Writing – review & editing:
Yanfang Qin, Jian Chen, Satish C. Singh

occurred (Figure 1). The complex rupture patterns of these events suggest the existence of a frictionally locked patch (Konca et al., 2008; Prawirodirdjo et al., 2010) that extends to more than 40 km depth (Chlieh et al., 2008).

Paleogeodetic, historical, and instrumental records of earthquakes along the Sumatran margin reveal that the megathrust tends to rupture completely in supercycles of large-slip events (Natawidjaja et al., 2006; Philibosian et al., 2014, 2017; Sieh et al., 2008). In this area, great earthquakes ruptured most of the Mentawai region in 1797 ($M_w > 8$) and 1833 ($M_w > 8.5$) (Nalbant et al., 2005) (Figure 1). The 2007 M_w 8.4 earthquake did not rupture the entire source zone of the 1833 earthquake and hence did not release enough accumulated moment since 1833 (Konca et al., 2008). High coupling remains beneath the segment of the Mentawai Islands, excluding the patches under the Batu and Enggano Islands (Konca et al., 2008; Prawirodirdjo et al., 2010). In a study of corals, Sieh et al. (2008) suggested that the 2007 event represents the start of a series of large partial failures of the Mentawai section that will probably occur in the next several decades, and their inference is supported by the occurrence of the 2010 earthquake (Philibosian et al., 2012). Modeling results have suggested that the human and property losses might be equal to or greater than those suffered during the 2004 M_w 9.2 Sumatra–Andaman event (Borrero et al., 2006). Hence, there is a high potential for a large earthquake to occur in the near future in the unruptured area of the Mentawai segment, where the coupling coefficient (fraction of seismic slip on the fault) is >0.5 (e.g., Konca et al., 2008; Lorito et al., 2008; Prawirodirdjo et al., 2010).

The amplitude of earthquake-triggered tsunamis is directly linked to the vertical displacement of the seafloor, which is controlled by the depth and magnitude of earthquakes and the coseismic slip propagating to the subduction front (e.g., Geist & Oglesby, 2014). For instance, the absence of significant slip at shallow depths during the 2005 and 2007 earthquakes likely can explain the relatively moderate tsunamis generated by these earthquakes (Konca et al., 2007). Additionally, the behaviors of the coseismic slip during the megathrust rupture are influenced by the deformation structures at the accretionary prism, especially the shallow frontal part of the wedge (Loveless & Meade, 2011; Noda et al., 2013). Therefore, the subsurface structures at the wedge front might play a crucial role during the tsunami generation.

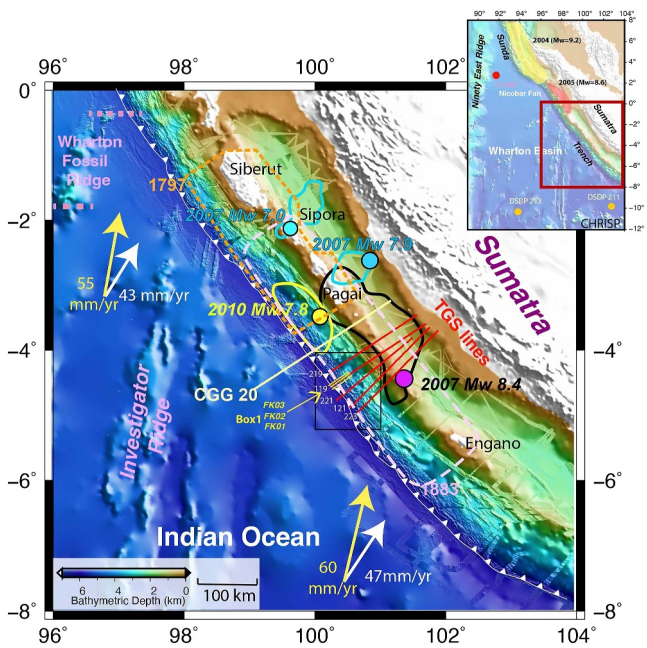

Figure 1. General tectonic setting of the Mentawai segment. The earthquake rupture areas in 1797 and 1833 are marked in orange dashed lines and pink dashed lines, respectively (Philibosian et al., 2014). The preferred coseismic slip model (yellow) of the 2010 M_w 7.8 event is from Hill et al. (2012). The 2007 earthquake sequence comprised three earthquakes: the M_w 8.4 Bengkulu (main shock, the black line encircles the rupture zone) and the M_w 7.9 Pagai-Sipora and M_w 7.0 subshock (rupture zones encircled by turquoise lines) events (e.g., Konca et al., 2008). Colored circles show event epicenters. The locations of the MCS profiles are shown by yellow and red lines. Convergence vectors (yellow arrows and numbers) and subduction velocities accounting for forearc motion (white arrows and numbers) are based on the studies of McNeill and Henstock (2014). The insert window shows the locations of drill sites. Yellow and red zones indicate the 2004 Sumatra-Andaman earthquake and 2005 Nias earthquake slip zones, respectively (e.g., Fujii et al., 2020, 2021).

Previous studies have shown that many different deformation structures near the trench axis can contribute to tsunami generation. During the 2011 Tohoku-Oki earthquake, seismic slip to the trench axis was associated with deformation structures linked to graben structures on the subducting plate (Fujiwara et al., 2011; Nakamura et al., 2013; Qin et al., 2022). The presence of low friction along the megathrust suggested by landward-vergent thrusts (Cubas et al., 2016) and thick incoming sediments in northern Sumatra (Moeremans et al., 2014) may have contributed to the rupture propagation near the subduction front during the 2004 earthquake (Gulick et al., 2011; Henstock et al., 2006; Singh et al., 2008). Recently, it has been suggested that bivergent pop-up structures were responsible for the tsunami generated by the 2010 M_w 7.8 Mentawai tsunami earthquake (Bradley et al., 2019; Hananto et al., 2020). These uncommon structures are considered to contribute to the propagation of rupture at shallow depths.

As mentioned above, the unruptured zone in the Mentawai segment holds a high potential for megathrust earthquakes in the near future. Subsurface structures, such as different vergences of deformation structures near the trench, have been suggested to influence shallow rupture propagation, consequently affecting the magnitude of an earthquake-triggered tsunami. Therefore, to assess the risk of an earthquake-triggered tsunami, it is crucial to investigate the subsurface structures along the trench. Here we use seismic reflection and bathymetric data from the central Mentawai region, southeast of the 2007 M_w 8.4 Mentawai earthquake and south of the 2010 M_w 7.8 tsunami earthquake (Figure 1), an area that has not ruptured in the recent past, to assess the potential risk of a future tsunami earthquake.

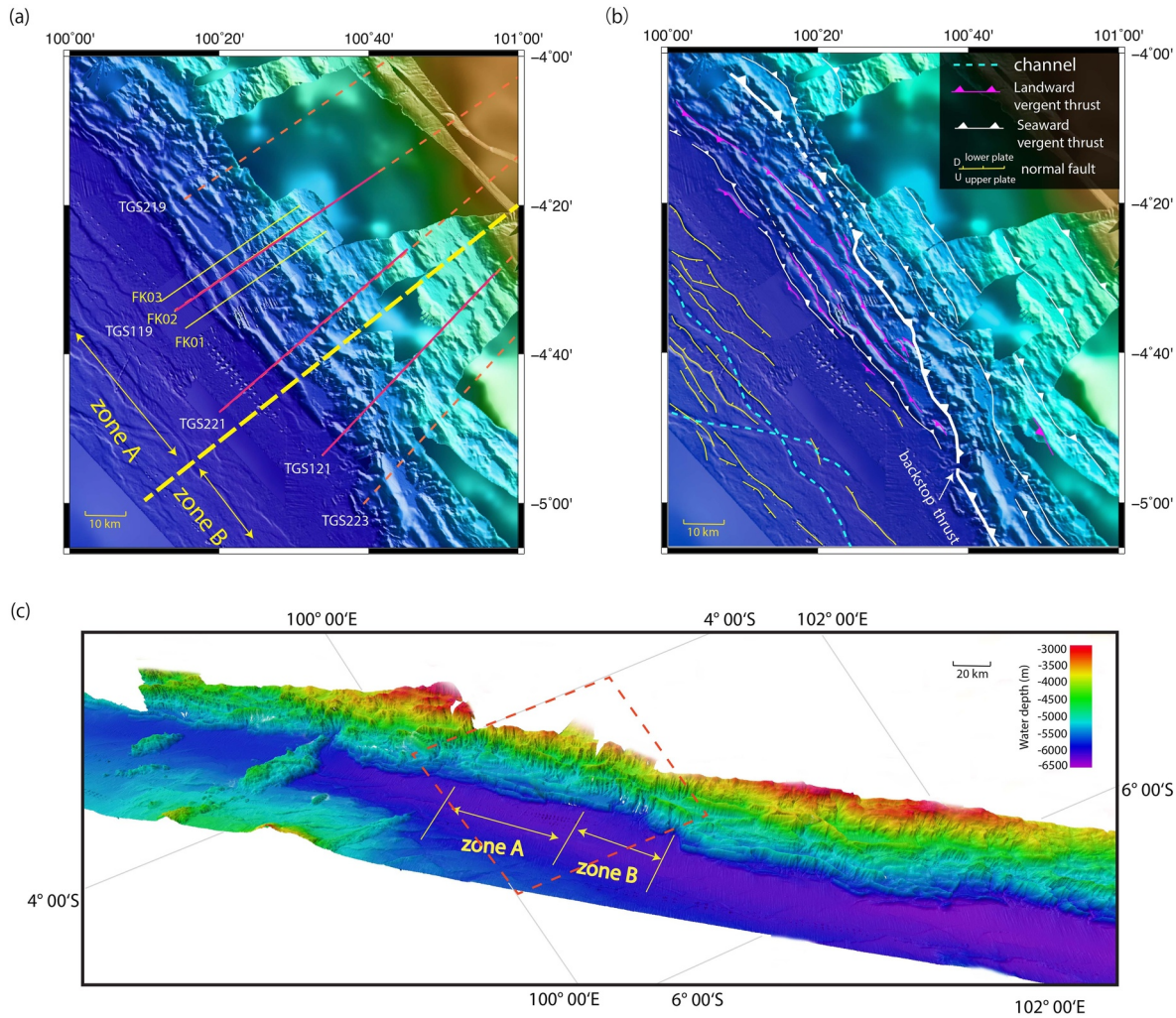

Figure 2. Morphology of the frontal accretionary wedge in our study area. (a) Map of the study area and locations of the seismic reflection profiles. The solid red parts of the TGS profiles indicate the parts discussed in this article. (b) Geological map based on interpretation of the bathymetry and showing tectonic features (normal faults, thrust faults, channels, etc.). (c) A 3D view of the high-resolution bathymetric map that includes the study regions in (a) and (b) (red dashed box) illustrates the outermost wedge topography along strike variability.

2. Seafloor Morphology

The high-resolution bathymetric data used in this study were collected in 2015 onboard R/V *Falkor* of the Schmidt Ocean Institute as part of the MegaTera (Mentawai Gap Tsunami Risk Assessment) project by a SIMRAD EM302 multibeam echo-sounder system with an operating frequency of 30 kHz. The bathymetric data were processed with CARIS HIPS software and gridded at ~25 m, and then combined with previous bathymetric data (Franke et al., 2008) (Figures 1 and 2).

In global view, the Sunda Trench deepens toward the southeast and separates a gently dipping outer rise from a steeply sloping accretionary prism (Figure 1). The along-trench sediments were derived from the accretionary prism or transported from the Bengal Fan. Central and south Sumatra are separated by the Investigator Ridge (Figure 1). The seafloor roughness is related to ridge and fracture zones in the Wharton Basin and the incoming sediments thin away from the Bengal Fan source offshore of southern Sumatra. The central part of the accretionary prism is narrow and steep, whereas in the south, the prism has a moderate width and slope. The deformation front step seaward, probably because roughness is diminished on the oceanic plate (McNeill & Henstock, 2014). The prism toe structures are mixed-vergence thrust folds, which

vary both along- and across-strikes in this zone (Kopp & Kukowski, 2003; Kopp et al., 2008; McNeill & Henstock, 2014).

In our study area, bend-related normal faults are observed in the southwest oceanic basin, ~20 km seaward of the trench (Figure 2b), similar to ones observed near the 2010 earthquake rupture zone further north (Hananto et al., 2020). The strikes of these normal faults are parallel to the wedge thrusts, indicating that activity due to the bending process is ongoing in this area. The bathymetry of the accretionary wedge shows rugged terrain in the study area, characterized by separated ridges or dome-like structures that confine sediments within underfilled basins (Figure 2). The most frontal deformational structures of the accretionary wedge are uneroded folds that lack large landslide deposits (Figure 2). The crests of the frontal ridges are slightly convex upward and tilt either landward or seaward. In the northern part of the study area (Figure 2b), the tilt is generally toward the trench, whereas in the southern part, it is away from the trench. The backstop thrust depicted in Figure 2b, shown as a seaward-vergent thrust, separates the smaller folds close to the trench with slight slopes (~2°) from the larger folds further landward with steeper slopes (6–8°) (Figure 2b). On the seaward side of this boundary thrust, the width of the gently dipping segment decreases from north to south, where younger sediments may be found. On the landward side of the boundary thrust, the deformation folds are much larger than those on the seaward side, indicating that the sediments are more ancient. Furthermore, this location is close to the point where the accretionary prism changes from steep and narrow to wider and less steep in south Sumatra (Figure 1) (McNeill & Henstock, 2014). This structural change may suggest the presence of a stress or friction transition in this region. Except in the southern part of the study area, juvenile fold crests near the trench tilt both landward and seaward, similar to folds observed elsewhere along the Sumatran margin (Bradley et al., 2019; Hananto et al., 2020).

3. Multichannel Seismic Reflection Data Imaging

During this study, we used three different types of multi-channel seismic (MCS) reflection data. Three short streamer seismic profiles, FK01, FK02, and FK03, with a line spacing of 6 km, were collected onboard R/V *Falkor* as a part of the MegaTera project. A 500 cubic inch (8.2 L) air-gun source was towed 3 m below the sea surface and fired every 25 m. A 1.2-km-long streamer with a 12.5-m receiver spacing towed at 4.5 m depth corresponded to a first-notch frequency of 167 Hz, providing a high-resolution seismic image. After denoising, the data were binned in common midpoint gathers every 6.25 m. A normal moveout correction was performed after velocity analysis, and the data were stacked, followed by post-stack Kirchhoff time migration. Because of the uncertainties caused by the velocity analysis of the short-streamer data, the depth conversion used an a priori velocity model developed from the CGG 20 and CGG 10 long-streamer profiles in the Mentawai region (Qin & Singh, 2018). This velocity model accounts for the increase in sediment velocity both with burial depth and distance downdip from the deformation front (larger degree of tectonic shortening). The horizontal trace spacing of the resulting data was 6.25 m, and the vertical resolution at a frequency of 100 Hz was 4 m. Profiles were surface-muted and gain-corrected for display and interpretation.

We also had access to data from five trench-orthogonal MCS lines acquired by the TGS company (TGS219, TGS119, TGS221, TGS121, and TGS223). These lines traverse the entire accretionary prism and forearc basin of the southern Mentawai region with a line spacing of ~20 km (Figure 1) These data were acquired with a 7.95-km-long streamer towed at 7 m depth and a 3940 cubic-inch air gun source towed at 5 m depth. The shot spacing was 37.5 m, and the record length was 12 s. The data were processed using a Kirchhoff pre-stack time migration workflow (Mukti et al., 2012). In this study, we used only selected portions of these seismic profiles (shown in Figure 2a) to discuss features of interest.

We also had access to data from a 15-km-long streamer seismic profile acquired by the CGG company. The CGG 20 profile was shot in 2009 using a tuned air-gun source with a total volume of 9600 cubic inches and three streamers. One streamer was 15 km long and towed at 22.5 m water depth, and the other two were 6 km long and towed at 7.5 and 15 m water depth. The source was deployed at 15 m depth and shot at 50-m intervals, and the record length was 20 s. The data from all three streamers were combined to obtain a broadband seismic response (Singh et al., 2011) and then processed using the pre-stack Kirchhoff depth-migration technique. Details on data acquisition and processing are given in Singh et al. (2011). Profile CGG 20 traverses the rupture patches of the 2007 and 2010 earthquakes (Figure 1).

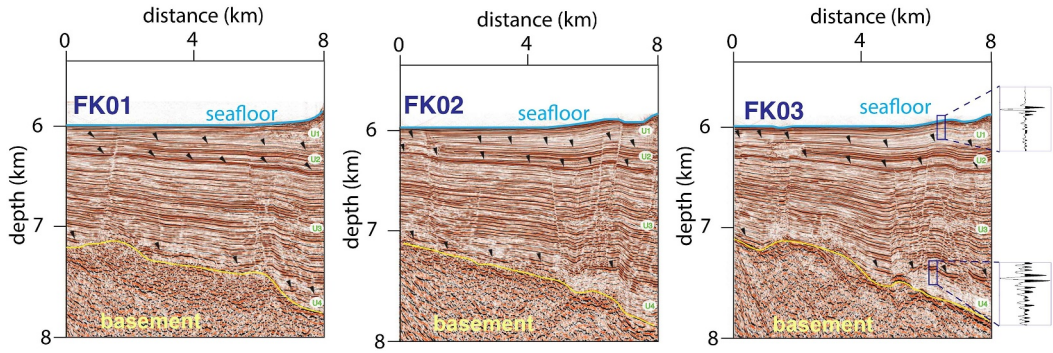

Figure 3. Seismic stratigraphy of the incoming sediments based on the depth-converted FK01, FK02, and FK03 profiles. Black arrows indicate boundaries between units U1–U4.

4. Interpretation of the Seismic Profiles

4.1. Seismic Stratigraphy

The N-S fractured Indian–Australian composite oceanic crust was formed by the spreading of Wharton Ridge (Jacob et al., 2014) during the Cretaceous. The sedimentary cover on the plate has been documented by a small number of reflection seismic profiles (e.g., Geersen et al., 2015) supported by sparse coring (Figure 1) (e.g., McNeill et al., 2017; Von der Borch et al., 2007). Because our study area is located north of the Christmas Island Seamount Province (CHRISP) (Hoernle et al., 2011), the lowest sediments covering the basaltic crust probably are volcaniclastic sediments rich in iron oxide minerals and pyrite that may be related to the active spreading ridges, as reported by the Deep Sea Drilling Project (DSDP) Leg 22 site 211 and Integrated Ocean Drilling Program U1480 (McNeill et al., 2017; Pickering et al., 2020; Von der Borch et al., 2007). Moving upward, it appears to consist of silt, sand, and clay that represent the turbiditic sediments from the Nicobar Fan in the North (Von der Borch et al., 2007).

We divide the incoming sedimentary layers into four units (U1–U4, from shallowest to deepest) according to the typical stratigraphy along profiles FK01–FK03 (Figure 3) by considering reflector truncation patterns and seismic reflectivity characteristics: The shallowest unit (U1) is a trench-fill sequence sourced by both along-trench transport from the northwest and mass wasting of the inner slope. U1 thins seaward and thickens into the wedge and is uplifted in frontal folds. This unit comprises homogeneously reflective internally divergent reflectors that exhibit angular discordance with the underlying sediments. Its maximum thickness is more than 200 m at the trench axis. Unit 2 (U2) consists of a sequence of layers with high seismic reflectivity characterized by planar reflections. Its thickness is almost constant (~200 m) near the trench axis, but it slightly thins seaward (Figures 4 and 5b), suggesting an increase in sediment accumulation rates towards the deformation front. Unit 3 (U3) is the thickest single unit; it is 1.2 km thick at the trench axis and thins seaward to several hundred meters. This unit exhibits weak-to-strong amplitude and planar-parallel reflectivity and hosts most of the normal faults (Figures 3 and 4). The thickness of the sediment-covered crust in this zone is ~4–5 km (~2s two-way travel time, Figure S1 in Supporting Information S1 and CGG 20 profile) according to the partially imaged oceanic Moho along profiles TGS121 and 221 (Figure 5).

A bright reflector with positive polarity separates units 3 and 4 (U4) (Figure 3), potentially representing an extended décollement. Although this may indicate different characteristics as compared to the northern Sumatra, where the proto-décollement shows a strong negative polarity (Dean et al., 2010; Qin & Singh, 2017; Stevens et al., 2021), the thinner incoming sediments in our study area could lead to different thermal conditions and local mineral compositions at depth. Factors such as cementation processes, possible lower porosity, and fluid content due to the absence of a low permeability cap layer may all contribute to varied seismic reflection patterns. On the other hand, if this proto-décollement layer is thin enough, it will function as a simple lithology boundary in the seismic data. The seismic transparency of U4 may be due to the presence of a pelagic sequence, such as nannofossil claystones and oozes (Von der Borch et al., 2007), and heterolithic sediments deposited on oceanic crust (e.g., Bradley et al., 2019). The thickness of this unit varies from dozens to hundreds of meters depending on the shape of the oceanic basement. The basement is defined by a low-frequency positive-polarity reflector that

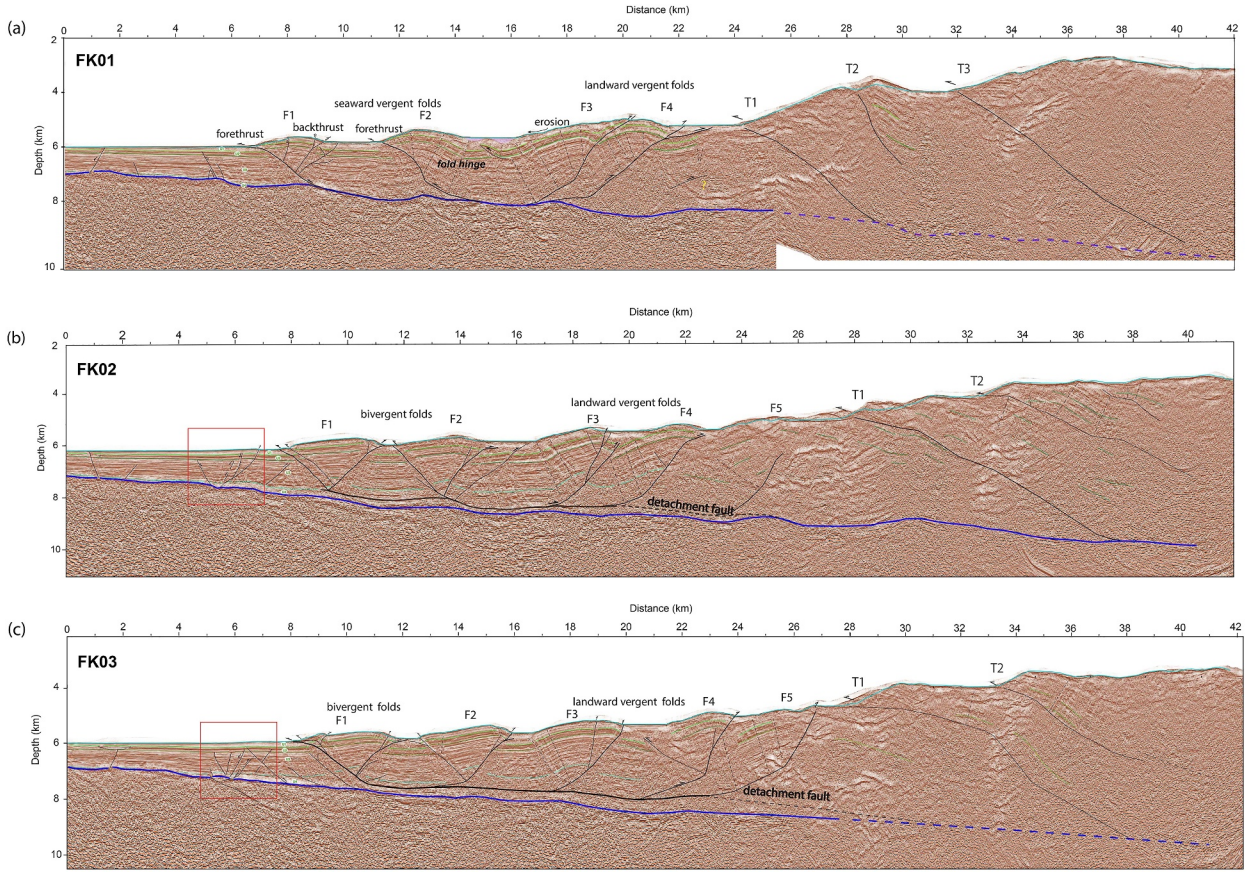

Figure 4. Depth-converted Kirchhoff time-migrated seismic images along profiles (a) FK01, (b) FK02, and (c) FK03 with interpretations. Blue lines mark the top of the subducting basement. Black lines indicate interpreted faults, dashed black lines are fold hinges, and green lines show the traces of continuous sedimentary layers (U1–U4). F1–F5 indicate anticlinal folds identified along the wedge. T1–T3 indicate seaward vergent thrusts identified along the prism. The red boxes in (b) and (c) indicate the windows that are blown up in Figure S2 of the Supporting Information S1. The vertical exaggeration is 1.

separates overlying planar reflectors of stratified sediments from underlying disorganized chaotic reflections. The boundary between U3 and U4 sometimes pinches out against topographic high structures in the basement.

4.2. Deformation of the Accretionary Prism

Some normal faults and thrust faults are observed in the incoming sediments along our seismic profiles before reaching the wedge (Figures 4 and 5; Figure S1 in Supporting Information S1), but most of these faults do not cut the entire sedimentary layer up to the seafloor, as shown in the bathymetric map (Figure 2). This finding suggests that most of these faults may result from upward propagation from deeper areas. The conjugated thrust faults near the toe of the prism show an early stage of folding structure development (Figure S2 in Supporting Information S1). In the future, they might rise to form new anticlines and develop into the toe of the prism (e.g., Figures 4b and 4c; Figure S2 in Supporting Information S1).

Profile CGG20 shows a cross-section of the whole accretionary prism and forearc basin (Figure 6; Figure S3 in Supporting Information S1). The whole prism can be divided into three parts: the lower, middle, and higher slopes according to the slope variation in the forearc region (e.g., Cook et al., 2014). Its features are consistent with those of the FK and TGS profiles. The detailed subsurface structures in the lower slope are clearly imaged by the short streamer data (Figures 4 and 5). Throughout the frontal prism, a clear complex structural vergence of ramp thrusts (Figures 4 and 5), consisting of steep and conjugate thrust fault pairs (forethrust/backthrust, McClay, 1992), is seen in the toe of the prism (e.g., F1 in Figure 4). These bivergent thrust folds, which may be tilted either landward or seaward, are dominant frontal features in our study area, along with imbricate sedimentary sequences that thicken toward the middle slope of the prism. Further landward, the structure consists of landward thrusts

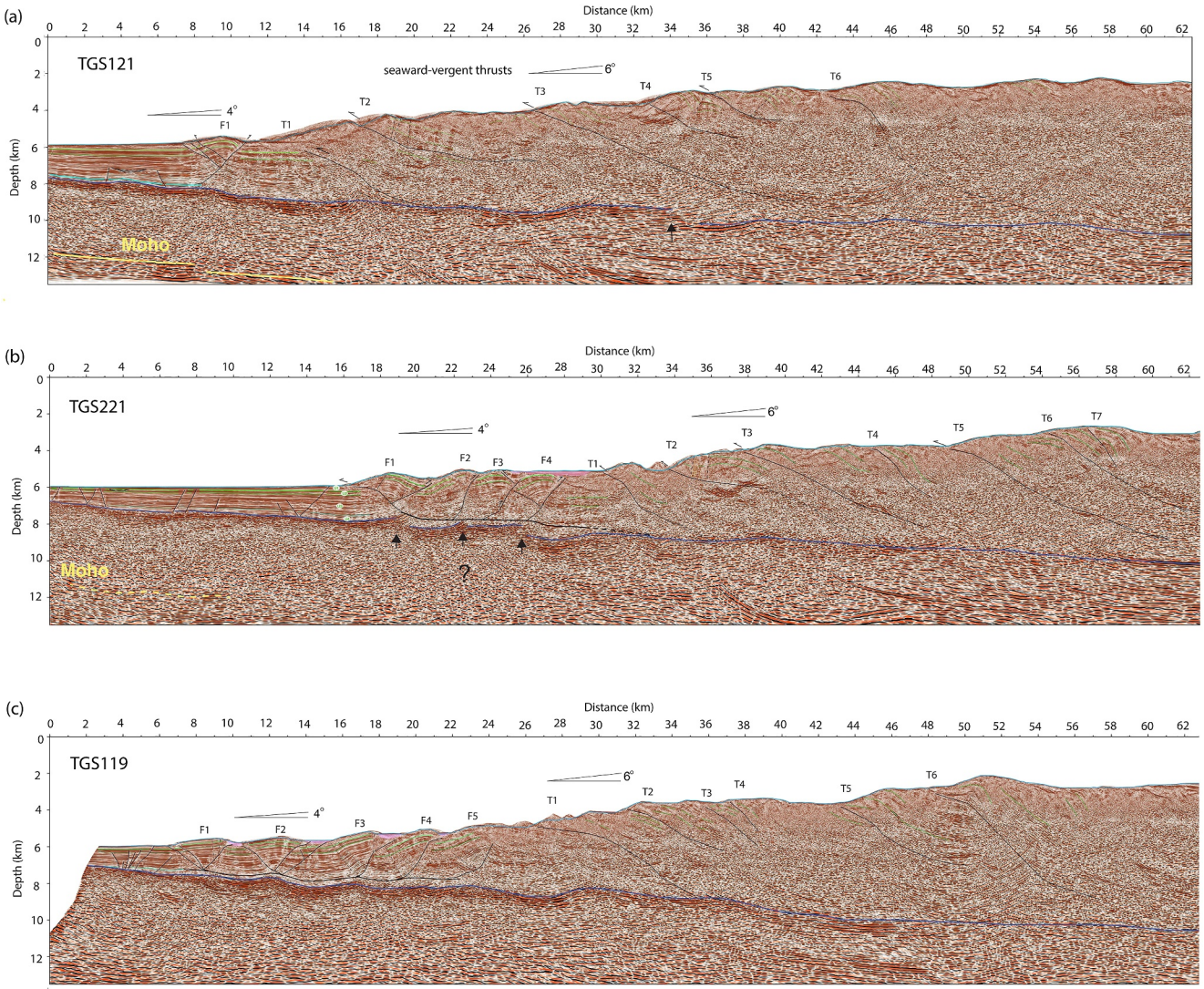

Figure 5. Depth-converted Kirchhoff time-migrated seismic images along profiles TGS121, TGS221, and TGS119 with interpretations. F1–F5 indicate anticlinal folds identified along the wedge. T1–T7 indicate seaward vergent thrusts identified along the prism. The thick black arrows in (a) and (b) mark the rough surface of the downgoing plate. The vertical exaggeration is 1.

dominated by flexural slip fault-bend folds (e.g., F3–F5 in Figure 4), which are defined by a ramp anticline with a dip panel separating an active axial surface that bisects the bedding angle from a subparallel inactive axial surface. The ramp anticlines are 3–4 km wide and occur at intervals of 1–2 km, with the gaps filled by mass wasting of the

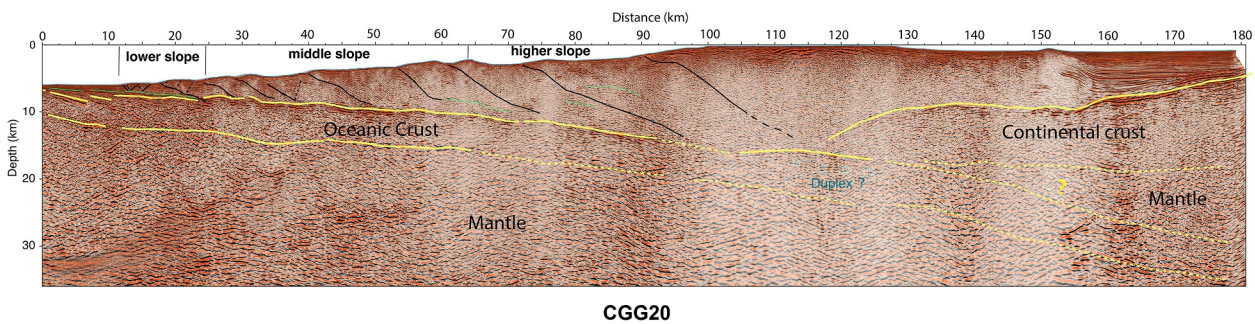

Figure 6. Depth-converted migrated seismic reflection image along profile CGG20 with interpretations. The vertical exaggeration is 1.

inner crest. The whole sequence of bivergent and landward thrust folds is ∼10–20 km long and deforms the sediment pile above the main basal décollement, which dips at ∼4–6° parallel to the top of the oceanic crust reflector. The main basal décollement is not itself a distinctive seismic reflector, and instead is interpreted as the estimated detachment fault connecting the roots of the frontal thrust faults (Bradley et al., 2019; Suppe, 1983). The FK01 profile is distinctive, because the frontal thrusts root directly on the plate interface. These thrusts are dominantly seaward-vergent rather than bivergent, with a larger anticline separation of ∼3 km and partially filled slope basins.

Further landward in the middle slope (surface seafloor slope of ∼6°), the large and laterally continuous thrust faults are primarily seaward-vergent that associated with ramp anticlines (Figure 5; Figure S1 in Supporting Information S1). The sediments in the middle slope are highly deformed, and it is not easy to trace the continuous strata. The outermost seaward thrust (T1 in Figures 4 and 5), forming the first seaward-vergent fold, separates the old sediments from the newer accreted sediments, each showing distinct characteristics. This thrust acts as the current backstop in the prism, deviating from the traditional role attributed to the Mentawai fault, which is located further landward and is defined as a tectonic structure with significantly greater strength than the more trenchward sedimentary sequence (e.g., Byrne et al., 1993; Silver et al., 1985). This dynamic backstop can strongly influence sediment accretion and earthquake rupture processes (e.g., Tsuji et al., 2015), and works as the out-of-sequence thrust that contributes to uplift of the outer forearc high (Gulick et al., 2011). The seafloor slope differs on either side of this boundary: the slope of the younger sediments in the lower slope, which host the landward and mixed vergent folds, is ∼4°, whereas the slope of the highly deformed older sediments deformed by seaward-vergent folds is ∼6°. However, our data poorly imaged this fault plane, and we can trace it just by discontinuities in the sedimentary layers, which is quite different from those showing bright seismic reflectors in other subduction zones, such as the Nankai subduction zone (e.g., Park et al., 2002).

The number of bivergent and landward-vergent folds in the lower slope decreases from north to south (FK03[5 folds] → FK02/TGS119[5 folds] → FK01[4 folds] → TGS221[4 folds] → TGS121[1 fold]) over our study area (Figures 4 and 5; Figure S1 in Supporting Information S1). In the north, ancient seaward-dipping thrusts (Ti) are first seen at 25–30 km landward from the trench, but as one moves south, the locations of thrust T1 move closer and closer to the trench axis. This observation is also supported by the seafloor topography, which shows that the slope of the prism surface increases southward from zone A (∼4°) to zone B (∼6°) (Figure 2c). Furthermore, the thickness of the incoming sediments in the trench increases from north to south along the strike (Figure S1 in Supporting Information S1), from ∼1.5 to ∼3 km; this increase might be linked to the seafloor topography and the fold vergences. In addition, some irregular faulting is associated with subducting topographic high features (Figure 5, TGS221) that seem to be linked to the landward vergent thrusts. Considered together, all these features suggest that the basal friction along the plate interface varies along the strike.

5. Sandbox Numerical Modeling

The typical seaward vergence of (landward-dipping) thrust faults in accretionary wedges arises primarily by rotation of principal stresses due to basal traction on a frictional décollement (Davis & Engelder, 1985). In contrast, if the subducting crust has a smooth topography, wedges that exhibit simultaneous shortening on both landward- and seaward-vergent faults or consistent landward-vergence are characterized by low basal traction and a low degree of internal stress rotation (Bonini, 2007). Systematic patterns of thrust vergence are therefore potential indicators of spatially variable mechanical properties of the décollement, which might be implicated in shallow rupture scenarios. To get an idea of how these physical parameters vary along the strike in our study region, we performed sandbox simulations using the discrete element method (DEM).

A DEM simulation models soil grains and rocks as individual elements in the form of spherical or non-spherical particles, and predicts particle trajectories by solving Newton–Euler equations of their motion (Cundall & Strack, 1979; Matuttis & Chen, 2014) (see Supporting Information S1). Instead of prescribing constitutive relations between stresses and strains, the forces and torques of contacting particle pairs are calculated using a combination of spring, dashpot, and slider models. In geology, DEM simulation models have been used to study the deformation properties of soft and hard rocks (Scholtès & Donzé, 2013) and to perform numerical sandbox experiments (Egholm, 2007; Furuichi et al., 2018), not only by reproducing laboratory experiments at the same resolution but also by providing additional information, such as the stress distribution, inside the box that is difficult to assess through physical experiments (Furuichi et al., 2018).

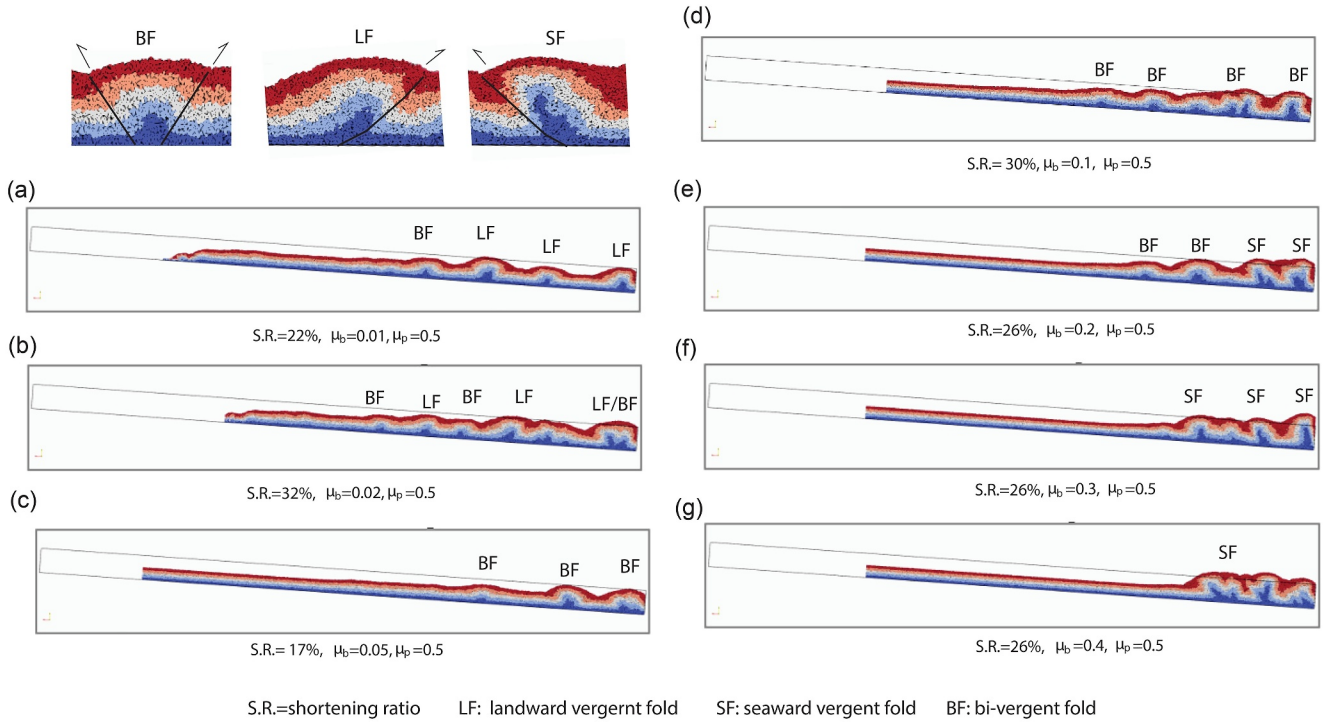

Figure 7. The DEM numerical simulation results for different shortening stages of the numerical sandbox experiments. The samples on the top left indicate the rule for interpretation of different deformation vergences. The vertical to horizontal aspect ratio is 1:1; the tilted rectangular box (gray lines) indicates the initial configuration with twice the initial filling depth before shortening; and the colors indicate particles with different initial depths. (a–g) simulation results based on the settings of internal/interparticle friction μ_p is fixed at 0.5 with basal friction μ_b increasing from 0.01 to 0.4. The shortening stages were manually selected from the output sequences of the simulations that generated a sufficient number of characteristic folds.

Here, to model the sediments, we used particles with a uniform size distribution among a maximum radius of 0.5 mm and a minimum radius of 0.41 mm. For simplicity, we assumed a homogeneous sand unit at the bottom of the box and modeled a basal décollement with low friction. In the simulation results (e.g., Figure 7), the strata are colored according to their initial depths to make the deformation patterns easier to see. The shortening of the sandbox is modeled by pushing the backstop wall at a shortening rate of 0.5 cm/s. The initial sediment depth D_0 was 2 cm and the length L_0 was 50 cm, with a relative depth scale of 1:25. The width was set to $W_0 = 0.5$ cm along the z- (trench) direction and the boundary condition was set to be periodic. In DEM simulations, a periodic boundary condition along the z-direction with a length W_0 means that every particle exiting at $z = W_0$ will appear at $z = 0$, and vice versa, thereby essentially extending the z dimension of the model to infinity. As in typical analog sandbox experiments (e.g., Dominguez, Lallemand, Malavieille, & von Huene, 1998; Lallemand et al., 1992), 1 cm in our simulation can be considered equivalent to 1 km in nature. For a more detailed discussion of model similarity, see Hubbert (1937). Instead of a specific length scale, our focus is on the deformation relative to the initial model size, that is, the (dimensionless) shortening ratio (S.R.) to the initial length caused by the loading from the backstop. The parameters used in the DEM simulation are listed in Table 1. The sediment parameters (Young's modulus E, Poisson's ratio ν, restitution coefficient e, and interparticle friction μ_p) were used to determine the parameters in the nonlinear spring (Hertz, 1881; Mindlin, 1949), dashpot, and Coulomb slider models. These sediment parameters were chosen by referring to the numerical sandbox experiments of Furuichi et al. (2018). Following previous modeling studies (e.g., Cubas et al., 2016), we considered several basal friction scenarios in this study: extremely low friction scenarios ($\mu_b = 0.01$, $\mu_b = 0.02$, and $\mu_b = 0.05$); a medium friction scenario ($\mu_b = 0.1$); and high friction scenarios ($\mu_b = 0.2$, $\mu_b = 0.3$, and $\mu_b = 0.4$). We set up two simple sandbox models to investigate the influence of the décollement dip and friction on the deformation of the accretionary prism. One sandbox was placed on a flat base, and the other was tilted at an angle $\beta = 4°$ (Figure S4 in Supporting Information S1). When the basal friction was small, this dip angle affected the locations and directions of local structures, as well as the number of folds; as the basal friction increased, the dip angle affected only the vergence

Table 1
DEM Parameters Used in Numerical Sandbox Experiments

Gravitational acceleration g	9.80665 m/s^2
Particle density ρ	2,700 kg/m^3
Young's modulus E	1×10^7 Pa
Poisson ratio ν	0.2
Coefficient of restriction e	0.2
Coefficient of friction μ_p between sand particles	0.5, 0.4,0.3
Coefficient of friction μ_b between sand and floor	0.01,0.02, 0.05,0.1, 0.2,0.3,0.4
Particle radius	0.5 * U (0.82, 1.0) mm
{Length L_0, Thickness D_0, Width W_0}	{500, 20, 5 mm}
Horizontal shortening rate v_h	5 mm/s
Décollement dip angle β	0° and 4°

direction of the folds (Figure S5 in Supporting Information S1). In the following section, we discuss only the cases with $\beta = 4°$, which were consistent with our field observations.

The numerical simulation results of the numerical sandbox experiments at different shortening stages are presented in Figures 7 and 8. The influence of the basal friction on local structure formation under a fixed interparticle friction can be observed from Figure 7, where the same interparticle friction $\mu_p = 0.5$ is set for different basal friction scenarios with μ_b ranging from 0.01 to 0.4. At low $\mu_b = 0.01$, 0.02, only landward vergent folds and very few bivergent folds are produced initially. As μ_b increases to 0.05 and 0.1, the number of bivergent folds increases, while the number of landward vergent folds decreases. The positions of the newly created folds were distributed randomly in the whole model, with a relative spare distribution. As time passed, folds with mixed vergences were observed (see Supporting Information S1). When the simulation used a higher basal friction value $\mu_b = 0.2$ (Figure 7e), bivergent and seaward vergent folds were generated. The distribution of seaward vergent folds is near the backstop, and bivergent folds are located trenchward. With higher μ_b values (Figures 7f and 7g), only seaward-vergent folds were generated, and the growth direction was continuous from the backstop, with a much narrower region of activity than in the low-friction cases. We also investigated the influence of the interparticle friction on local structure formation under a fixed basal friction (Figure 8). When the basal friction was fixed at $\mu_b = 0.1$ and the interparticle friction was varied ($\mu_p = 0.5$, 0.4, and 0.3), we found that the interparticle friction value μ_p influences both the fold dipping directions and the positions of fold generation. As μ_p decreases, at the same shortening ratio, the distribution of the active folds widens, and these folds generally show similar patterns (dominantly bivergent).

The numerical modeling used more controlled conditions to investigate specific frictional parameters, so the frictional behaviors observed in a sandbox may not precisely reflect the full range of frictional complexities present in the earth. Nevertheless, the experiment can capture essential qualitative aspects and provide an intuitive understanding of the subduction process. Here, the numerical simulation results indicate that both internal and basal friction influence the emergence of landward-vergent folds. The seismic data show similar deformed patterns in the subsurface over the whole study area, indicating that the internal friction should be more or less homogeneous in our study area, because the composition of the accretionary prism is similar, and the speed of the subducting slab does not vary much. The outer wedges of FK03,FK02/TGS119,FK01 show similar patterns to the modeling results with low basal friction (Figures 7a and 7b). Although profile TGS221 shows bivergent and landward vergent folds at the prism front, these folds are close to each other and are associated with a narrower section of the prism than the northern profiles. The southernmost profile, TGS121, is similar to the simulation with basal friction 0.2 case (Figure 7e). Therefore, considering both the numerical results and our observed seismic data, we inferred that the basal friction varies along strike, increasing from NW to SE and corresponding to the observed variation of the landward-vergent folds (zone A to zone B in Figure 2c).

6. Discussion

During the 2010 Mentawai tsunami earthquake, slip seems to have occurred coseismically on shallow ramps, causing uplift and enhancement in areas with a bivergent frontal structure (Bradley et al., 2019; Hananto et al., 2020; Satake et al., 2013; Yue et al., 2014). The northwestern part of our study region (north of 4°40′S) shows active bivergent thrust faults at the toe of the accretionary prism that are similar to structures found within the 2010 rupture zone (Bradley et al., 2019; Hananto et al., 2020) and thus might contribute to maximum uplift during a future tsunami earthquake. The region southeast of profile TGS221 (zone B) is dominated by seaward-vergent folds consisting of old sediments, with a steeper seafloor slope (~6°). The thickness of the incoming sediments increases to ~3 km. This increase in overburden pressure at depth enhances the compaction of sediment particles, indicating stronger basal traction. Therefore, it should function in a different way than in the more northward region (zone A). The fold vergence variation along the strike suggests that the plate compressional stress and basal friction may change at around 4°40′S, and this region could be a transition zone. According to the simulation results, the basal friction is lower in the northern region, and the décollement level is above the plate

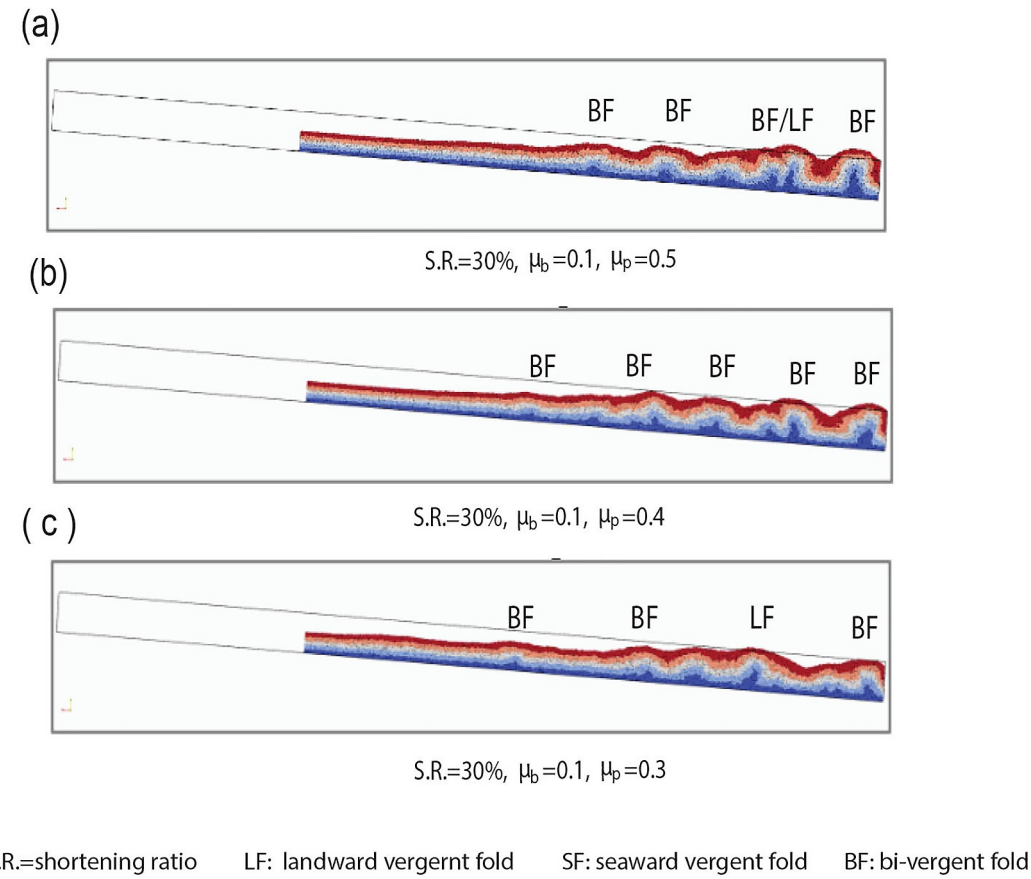

Figure 8. The DEM numerical simulation results for different shortening stages of the numerical sandbox experiments. The vertical to horizontal aspect ratio is 1:1; the tilted rectangular box (gray lines) indicates the initial configuration with twice the initial filling depth before shortening; and the colors indicate particles with different initial depths. (a–c) shows the simulation results by setting basal friction μ_b is fixed at 0.1 with internal/interparticle friction μ_p decreasing from 0.5 to 0.3. The shortening stages were selected at the same ratio 30%.

interface. However, in the south (south of ~5°20′S), the bathymetric data show young, accreted folds in the outer wedge again (Figure 1). Thus, the friction increases abruptly between 4°40′S and 5°20′S, and this increase might be linked to seamount subduction, as the prism toe morphology in this zone is similar to those places where the spreading center in the Wharton Basin, the Investigator Ridge, and some isolated seamounts are subducting (Figure S6 in Supporting Information S1 zones 1–3). In areas where these irregular topographic features subduct, the toe of the prism has been destroyed and the folded features are not continuous along the strike (e.g., Marcaillou et al., 2016; Xia et al., 2023). The same phenomenon can also be seen in modeling results (e.g., Dominguez, Lallemand, Malavieille, & von Huene, 1998) as well as in Costa Rica (e.g., Sak et al., 2009) and along the Ryukyu margin (e.g., Dominguez, Lallemand, Malavieille, & Schnürle, 1998). Therefore, the rough features on the downgoing plate beneath the wedge front along profile TGS221 might be related to reliefs on the incoming plate, which can introduce higher friction in the region and produce a trench reentrant pattern on the map.

The N-S continuous dynamic backstop thrust (T1) separating the lower and middle slopes of the wedge (Figure 2b) might directly affect the coseismic rupture processes. During the 2010 earthquake rupture, the largest displacement (3–6 m) occurred ~17 km landward from the trench, and then the displacement decreased rapidly further landward (Yue et al., 2014). This result indicates that there might be a mechanical difference between the frontal part and the inner landward part of the wedge, with a potential boundary separating young and old chaotic accreted sediments, due to consolidation, diagenesis, and lithification caused by increasing temperature and pressure (Moore & Saffer, 2001). This barrier is found as a seaward-dipping thrust in the rupture zone north of our study region (Figure S7 in Supporting Information S1, distance ~20 km), and it extends southward into our study area, where no rupture has occurred recently. This out-of-sequence seaward-dipping thrust is consistent from

north to south in both the seismic reflection data and the morphology indicated by the bathymetry. It contributes to the uplift of the outer forearc high; thus, it may currently act as a backstop and may be playing an important role in forearc evolution, and may be important for tsunami generation (e.g., Park et al., 2002).

Normally, frontal accretionary prism structures are expected to have less accumulated slip compared with inner structures during interseismic periods (e.g., Wang & Hu, 2006). However, during the 2010 earthquake, the largest amount of ramp fault displacement and surface uplift during near-trench coseismic slip seems to have occurred on the one to two most frontal structures (Hananto et al., 2020); this finding suggests that the most significant slip and deformation was accumulated on the most frontal ramp faults. Active frontal accretion and the seaward propagation of tectonic structures are demonstrated by the structures in the trench along FK02 and FK03 (Figures 4b and 4c; between 5 and 7 km distance), which show the development of potential thrust folds, including forethrusts and backthrusts. These features indicate that the recent deformation in the wedge dominantly broke forward, with active shortening being accommodated on the most frontal of the ramp thrusts. This mechanism is also supported by the low-friction sandbox simulations ($\mu_b < 0.05$) in which the young-stage folds are landward-dipping or bivergent. These active pre-existing faults act as zones of weakness in the trench, indicating a high stress field and facilitating the propagation of co-seismic ruptures during earthquakes (e.g., Nakamura et al., 2013). Furthermore, a low basal friction condition, associated with low fracture energy, could minimize spatial variation in frictional behavior, enhance slip-weakening distance and allow the rupture to propagate to the trench (Seyler et al., 2020). Hence, a rupture can propagate to the trench here during great earthquakes, even if the shallow megathrust is velocity strengthening and cannot itself nucleate ruptures.

The morphology and structure of the prism are controlled by many parameters, including the convergence rate, incoming sediment thickness, hydrological rate, and the subducting basement (e.g., Clift & Vannucchi, 2004; Saffer & Bekins, 2002). According to critical taper theory, the slope angle is related to the effective basal friction (Dahlen, 1984; Davis et al., 1983). The sum of the topographic slope and the megathrust dip varies from ∼8° to ∼10° from north to south in association with the increasing thickness of the incoming sediments, with dense and probably thermally strengthened sediments (e.g., Smith et al., 2013). The subduction of high-friction topographic structures in the southern study area is further evidenced by the presence of rare normal faults observed within the wedge. Continuous compression and uplift of the accretionary prism has occurred above the rough plate interface, which in this region is composed of discontinuous multiple faults that are offset vertically (Figure 5b, from 16 to 28 km distance) (Okuma et al., 2022). Higher internal friction can also lead to a thicker and steeper wedge (Figure 7), but the properties of the input sediments are not very different over the whole study area; therefore, the stress load due to the subduction of a rough downgoing plate may have caused an increase in internal friction (e.g., Ruh et al., 2016), which is another factor that might explain the lateral changes in the vergence of the frontal wedge.

Weak basal traction can lead to landward-dipping thrust folds and bivergent folds, and such structures at the front of the prism can contribute to a large tsunami, such as the 2004 Sumatra–Andaman M_w 9.1, the 1700 Cascadia (Cubas et al., 2016), and the 2010 Mentawai (Bradley et al., 2019; Hananto et al., 2020) earthquake tsunamis. These examples suggest that low-friction properties may play an important role during coseismic propagation and uplift of the seafloor. On the other hand, the décollement level is controlled by both the sedimentary lithology (Bradley et al., 2019) and the basal friction. Dewatering of clays may have led to a long-term increase in pore pressure along the proto-décollement (Dean et al., 2010; Geersen et al., 2013; Qin & Singh, 2017), along with thermal pressurization of pore fluids (Di Toro et al., 2011), and other processes causing dynamic weakening, which could lead to short-term pore fluid pressure elevation and affect the basal friction. Although the proto-décollement here shows normal seismic polarity, indicating the fluid pressure is not as high as the northern Sumatra (e.g., Stevens et al., 2021), might be due to the absence of a low permeability cap layer, or its thickness is much thinner etc. All of these processes are associated with effective friction variation. The higher basal friction in the southern area, which indicates that the décollement contains less water and is warmer there than in the northern region, may create a rupture barrier during coseismic propagation.

7. Conclusions

We have mapped subsurface deformation structures in the outer part of the accretionary prism in the unruptured central Mentawai segment. Our observations show detailed ramp fault vergence and the stratigraphic level of frontal décollements, as well as folds with mixed vergence in the toe of the prism; these features are similar to

those in the northern tsunami earthquake rupture zone. Our observations, together with basal friction test modeling, can help us to estimate areas where the risk of future large tsunami earthquakes is enhanced, such as the northern region of zone A. In this study region, there is a high possibility of future earthquakes to release the accumulated strain. If the coseismic slip could reach the prism front, the possibility of tsunami generation would be extremely high, and the southern boundary of this region (~5°S) may function as a slip barrier. Future observations of frontal accretionary wedges and incoming oceanic stratigraphy in areas that have experienced historical tsunamigenic earthquakes would further improve our understanding of the physical mechanisms underlying these damaging events.

Conflict of Interest

The authors declare no conflicts of interest relevant to this study.

Data Availability Statement

The data that support the findings of this study are openly available in the Marine Geoscience Data System (Rolling Deck to Repository (2015), https://doi.org/10.7284/901585). Migrated seismic profiles are available in Qin (2024), https://doi.org/10.5281/zenodo.10477365. The commercial license for the DEM software DEPTH is available from this vendor: https://www.advancesoft.jp/products/particle-method/advance_depth/. Academic collaboration is available from the authors upon reasonable request.

Acknowledgments
This paper is dedicated to the cherished memory of Paul Tapponnier. In remembrance of Paul, this work stands as a tribute to his enduring impact on our academic journey. Here we would like to thank the crew of the R/V Falkor cruise FK150523. Funding for MegaTera was provided by the Earth Observatory of Singapore. The MegaTera expedition was a joint project between the Earth Observatory of Singapore (EOS), the Indonesian Institute of Sciences (LIPI), the Institute de Physique du Globe de Paris (IPGP), and the Schmidt Ocean Institute (SOI). This research is partly supported by the National Research Foundation Singapore and the Singapore Ministry of Education under the Research Centres of Excellence initiative. This research is also supported by JSPS KAKENHI Grant JP24H01044.

References

Bonini, M. (2007). Interrelations of mud volcanism, fluid venting, and thrust-anticline folding: Examples from the external northern Apennines (Emilia-Romagna, Italy). *Journal of Geophysical Research*, *112*(B8), B08413. https://doi.org/10.1029/2006JB004859

Borrero, J. C., McAdoo, B., Jaffe, B., Dengler, L., Gelfenbaum, G., Higman, B., et al. (2011). Field survey of the March 28, 2005, Nias-Simeulue earthquake and tsunami. *Pure and Applied Geophysics*, *168*(6–7), 1075–1088. https://doi.org/10.1007/s00024-010-0218-6

Borrero, J. C., Sieh, K., Chlieh, M., & Synolakis, C. E. (2006). Tsunami inundation modeling for western Sumatra. *Proceedings of the National Academy of Sciences of the United States of America*, *103*(52), 19673–19677. https://doi.org/10.1073/pnas.0604069103

Borrero, J. C., Weiss, R., Okal, E. A., Hidayat, R., Suranto Arcas, D., & Titov, V. V. (2009). The tsunami of 2007 September 12, Bengkulu province, Sumatra, Indonesia: Post-tsunami field survey and numerical modelling. *Geophysical Journal International*, *178*(1), 180–194. https://doi.org/10.1111/j.1365-246X.2008.04058.x

Bradley, K., Qin, Y., Carton, H., Hananto, N., Villanueva-Robles, F., Leclerc, F., et al. (2019). Stratigraphic control of frontal décollement level and structural vergence and implications for tsunamigenic earthquake hazard in Sumatra, Indonesia. *Geochemistry, Geophysics, Geosystems*, *20*(3), 1646–1664. https://doi.org/10.1029/2018GC008025

Byrne, D. E., Wang, W., & Davis, D. M. (1993). Mechanical role of backstops in the growth of forearcs. *Tectonics*, *12*(1), 123–144.

Chlieh, M., Avouac, J.-P., Sieh, K., Natawidjaja, D. H., & Galetzka, J. (2008). Heterogeneous coupling of the Sumatran megathrust constrained by geodetic and paleogeodetic measurements. *Journal of Geophysical Research*, *113*, B5. https://doi.org/10.1029/2007jb004981

Clift, P. D., & Vannucchi, P. (2004). Controls on tectonic accretion versus erosion in subduction zones: Implications for the origin and recycling of the continental crust. *Reviews of Geophysics*, *42*(2), RG2001. https://doi.org/10.1029/2003RG000127

Cook, B. J., Henstock, T. J., McNeill, L. C., & Bull, J. M. (2014). Controls on spatial and temporal evolution of prism faulting and relationships to plate boundary slip offshore north-central Sumatra. *Journal of Geophysical Research: Solid Earth*, *119*(7), 5594–5612. https://doi.org/10.1002/2013JB010834

Cubas, N., Souloumiac, P., & Singh, S. C. (2016). Relationship link between landward vergence in accretionary prisms and tsunami generation. *Geology*, *44*(10), 787–790. https://doi.org/10.1130/g38019.1

Cundall, P. A., & Strack, O. D. L. (1979). A discrete numerical model for granular assemblies. *Géotechnique*, *29*(1), 47–65. https://doi.org/10.1680/geot.1979.29.1.47

Dahlen, F. A. (1984). Noncohesive critical Coulomb wedges: An exact solution. *Journal of Geophysical Research*, *89*(B12), 10125–10133. https://doi.org/10.1029/JB089iB12p10125

Davis, D., Suppe, J., & Dahlen, F. A. (1983). Mechanics of fold-and-thrust belts and accretionary wedges. *Journal of Geophysical Research*, *88*(B2), 1153–1172. https://doi.org/10.1029/JB088iB02p01153

Davis, D. M., & Engelder, T. (1985). The role of salt in fold-and-thrust belts. *Tectonophysics*, *119*(1–4), 67–88. https://doi.org/10.1016/0040-1951(85)90033-2

Dean, S. M., McNeill, L. C., Henstock, T. J., Bull, J. M., Gulick, S. P. S., Austin, J. A., et al. (2010). Contrasting decollement and prism properties over the Sumatra 2004-2005 earthquake rupture boundary. *Science*, *329*(5988), 207–210. https://doi.org/10.1126/science.1189373

Di Toro, G., Han, R., Hirose, T., De Paola, N., Nielsen, S., Mizoguchi, K., et al. (2011). Fault lubrication during earthquakes. *Nature*, *471*(7339), 494–498. https://doi.org/10.1038/nature09838

Dominguez, S., Lallemand, S., Malavieille, J., & Schnürle, P. (1998). Oblique subduction of the Gagua Ridge beneath the Ryukyu accretionary wedge system: Insights from marine observations and sandbox experiments. *Marine Geophysical Researches*, *20*(5), 383–402. https://doi.org/10.1023/a:1004614506345

Dominguez, S., Lallemand, S., Malavieille, J., & von Huene, R. (1998). Upper plate deformation associated with seamount subduction. *Tectonophysics*, *293*(3–4), 207–224. https://doi.org/10.1016/s0040-1951(98)00086-9

Egholm, D. L., Sandiford, M., Clausen, O. R., & Nielsen, S. B. (2007). A new strategy for discrete element numerical models: 2. Sandbox applications. *Journal of Geophysical Research*, *112*(B5), B05204. https://doi.org/10.1029/2006jb004558

Franke, D., Schnabel, M., Ladage, S., Tappin, D. R., Neben, S., Djajadihardja, Y. S., et al. (2008). The great Sumatra–Andaman earthquakes—Imaging the boundary between the ruptures of the great 2004 and 2005 earthquakes. *Earth and Planetary Science Letters*, *269*(1–2), 118–130. https://doi.org/10.1016/j.epsl.2008.01.047

Fujii, Y., Satake, K., Watada, S., & Ho, T. (2020). Slip distribution of the 2005 Nias earthquake (Mw 8.6) inferred from geodetic and far-field tsunami data. *Geophysical Journal International*, *223*(2), 1162–1171. https://doi.org/10.1093/gji/ggaa384

Fujii, Y., Satake, K., Watada, S., & Ho, T. C. (2021). Re-examination of slip distribution of the 2004 Sumatra–Andaman earthquake (Mw 9.2) by the inversion of tsunami data using green's functions corrected for compressible seawater over the elastic Earth. *Pure and Applied Geophysics*, *178*(12), 4777–4796. https://doi.org/10.1007/s00024-021-02909-6

Fujiwara, T., Kodaira, S., No, T., Kaiho, Y., Takahashi, N., & Kaneda, Y. (2011). The 2011 Tohoku-Oki earthquake: Displacement reaching the trench axis. *Science*, *334*(6060), 1240. https://doi.org/10.1126/science.1211554

Furuichi, M., Nishiura, D., Kuwano, O., Bauville, A., Hori, T., & Sakaguchi, H. (2018). Arcuate stress state in accretionary prisms from real-scale numerical sandbox experiments. *Scientific Reports*, *8*(1), 8685. https://doi.org/10.1038/s41598-018-26534-x

Geersen, J., Bull, J. M., McNeill, L. C., Henstock, T. J., Gaedicke, C., Chamot-Rooke, N., & Delescluse, M. (2015). Pervasive deformation of an oceanic plate and relationship to large >M_w8 intraplate earthquakes: The northern Wharton Basin, Indian Ocean. *Geology*, *43*(4), 359–362. https://doi.org/10.1130/G36446.1

Geersen, J., McNeill, L., Henstock, T. J., & Gaedicke, C. (2013). The 2004 Aceh-Andaman Earthquake: Early clay dehydration controls shallow seismic rupture. *Geochemistry, Geophysics, Geosystems*, *14*(9), 3315–3323. https://doi.org/10.1002/ggge.20193

Geist, E. L., & Oglesby, D. D. (2014). Earthquake mechanism and seafloor deformation for tsunami generation. In M. Beer, I. Kougioumtzoglou, E. Patelli, & I. K. Au (Eds.), *Encyclopedia of earthquake engineering*. Springer. https://doi.org/10.1007/978-3-642-36197-5_296-1

Gulick, S., Austin, J., McNeill, L., Bangs, N., Martin, K., Henstock, T., et al. (2011). Thick indurated sediments extend updip rupture propagation during 2004 Sumatra earthquake. *Nature Geoscience*, *4*(7), 453–456. https://doi.org/10.1038/NGEO117

Hananto, N. D., Leclerc, F., Li, L., Etchebes, M., Carton, H., Tapponnier, P., et al. (2020). Tsunami earthquakes: Vertical pop-up expulsion at the forefront of subduction megathrust. *Earth and Planetary Science Letters*, *538*, 116197. https://doi.org/10.1016/j.epsl.2020.116197

Henstock, T., McNeill, L., & Tappin, D. (2006). Seafloor morphology of the Sumatran subduction zone: Surface rupture during megathrust earthquakes? *Geology*, *34*(6), 485–488. https://doi.org/10.1130/22426.1

Hertz, H. (1881). Ueber die Berührung fester elastischer Körper. *Journal für die Reine und Angewandte Mathematik*, *92*, 156–171. https://doi.org/10.1515/crll.1882.92.156

Hill, E. M., Borrero, J. C., Huang, Z., Qiu, Q., Banerjee, P., Natawidjaja, D. H., et al. (2012). The 2010 M_w 7.8 Mentawai earthquake: Very shallow source of a rare tsunami earthquake determined from tsunami field survey and near-field GPS data. *Journal of Geophysical Research*, *117*(B6), B06402. https://doi.org/10.1029/2012JB009159

Hoernle, K., Hauff, F., Werner, R., van den Bogaard, P., Gibbons, A. D., Conrad, S., & Muller, R. D. (2011). Origin of Indian Ocean Seamount Province by shallow recycling of continental lithosphere. *Nature Geoscience*, *4*(12), 883–887. https://doi.org/10.1038/ngeo1331

Hubbert, M. K. (1937). Theory of scale models as applied to the study of geological structures. *Bulletin of the Geological Society of America*, *48*(10), 1459–1520. https://doi.org/10.1130/gsab-48-1459

Jacob, J., Dyment, J., & Yatheesh, V. (2014). Revisiting the structure, age, and evolution of the Wharton Basin to better understand subduction under Indonesia. *Journal of Geophysical Research: Solid Earth*, *119*(1), 169–190. https://doi.org/10.1002/2013JB010285

Konca, A. O., Avouac, J.-P., Sladen, A., Meltzner, A. J., Sieh, K., Fang, P., et al. (2008). Partial rupture of locked patch of the Sumatra megathrust during the 2007 earthquake sequence. *Nature*, *456*(7222), 631–635. https://doi.org/10.1038/nature07572

Konca, A. O., Hjorleifsdottir, V., Song, T. R. A., Avouac, J. P., Helmberger, D. V., Ji, C., et al. (2007). Rupture kinematics of the 2005, M_w 8.6, Nias-Simeulue earthquake from the joint inversion of seismic and geodetic data. *Bulletin of the Seismological Society of America*, *97*(1A), S307–S322. https://doi.org/10.1785/0120050632

Kopp, H., & Kukowski, N. (2003). Backstop geometry and accretionary mechanics of the Sunda margin. *Tectonics*, *22*(6), 1072. https://doi.org/10.1029/2002TC001420

Kopp, H., Weinrebe, W., Ladage, S., Barckhausen, U., Klaeschen, D., Flueh, E. R., et al. (2008). Lower slope morphology of the Sumatra trench system. *Basin Research*, *20*(4), 519–529. https://doi.org/10.1111/j.1365-2117.2008.00381.x

Lallemand, S. E., Malavieille, J., & Calassou, S. (1992). Effects of oceanic ridge subduction on accretionary wedges: Experimental modeling and marine observations. *Tectonics*, *11*(6), 1301–1313. https://doi.org/10.1029/92tc00637

Lay, T., Kanamori, H., Ammon, C. J., Nettles, M., Ward, S. N., Aster, R. C., et al. (2005). The great Sumatra-Andaman earthquake of 26 December 2004. *Science*, *308*(5725), 1127–1133. https://doi.org/10.1126/science.1112250

Lorito, S., Romano, F., Piatanesi, A., & Boschi, E. (2008). Source process of the September 12, 2007, M_w 8.4 southern Sumatra earthquake from tsunami tide gauge record inversion. *Geophysical Research Letters*, *35*(2), 1–6. https://doi.org/10.1029/2007gl032661

Loveless, J. P., & Meade, B. J. (2011). Spatial correlation of interseismic coupling and coseismic rupture extent of the 2011 M_w=9.0 Tohoku-oki earthquake. *Geophysical Research Letters*, *38*(17), L17306. https://doi.org/10.1029/2011GL048561

Marcaillou, B., Collot, J. Y., Ribodetti, A., Acremont, E., Mahamat, A. A., & Alvarado, A. (2016). Seamount subduction at the North-Ecuadorian convergent margin: Effects on structures, inter-seismic coupling and seismogenesis. *Earth and Planetary Science Letters*, *433*, 146–158. https://doi.org/10.1016/j.epsl.2015.10.043

Matuttis, H.-G., & Chen, J. (2014). *Understanding the discrete element method: Simulation of non-spherical particles for granular and multi-body systems*. John Wiley & Sons.

McClay, K. R. (1992). In K. R. McClay (Ed.), *Thrust tectonics* (pp. 419–433). Chapman & Hall.

McNeill, L. C., Dugan, B., Petronotis, K. E., Backman, J., Bourlange, S., Chemale, F., Jr., et al. (2017). *Proceedings of the International Ocean Discovery Program; Sumatra subduction zone; Expedition 362 of the riserless drilling platform, Colombo, Sri Lanka, to Singapore; Sites U1480-U1481, 6 August–6 October 2016*. https://doi.org/10.7289/V5C8276M

McNeill, L. C., & Henstock, T. J. (2014). Forearc structure and morphology along the Sumatra-Andaman subduction zone. *Tectonics*, *33*(2), 112–134. https://doi.org/10.1002/2012TC003264

Mindlin, R. (1949). Compliance of elastic bodies in contact. *Journal of Applied Mechanics*, *16*(3), 259–268. https://doi.org/10.1115/1.4009973

Moeremans, R., Singh, S., Mukti, M., McArdle, J., & Johansen, K. (2014). Seismic images of structural variations along the deformation front of the Andaman–Sumatra subduction zone: Implications for rupture propagation and tsunamigenesis. *Earth and Planetary Science Letters*, *386*, 75–85. https://doi.org/10.1016/j.epsl.2013.11.003

Moore, J. C., & Saffer, D. M. (2001). Updip limit of the seismogenic zone beneath the accretionary prism of southwest Japan: An effect of diagenetic to low-grade metamorphic processes and increasing effective stress. *Geology*, *29*(2), 183–186. https://doi.org/10.1130/0091-7613(2001)029<0183:ulotsz>2.0.co;2

Mukti, M. M., Singh, S. C., Deighton, I., Hananto, N. D., Moeremans, R., & Permana, H. (2012). Structural evolution of backthrusting in the Mentawai Fault Zone, offshore Sumatran forearc. *Geochemistry, Geophysics, Geosystems*, *13*(12), Q12006. https://doi.org/10.1029/2012GC004199

Nakamura, Y., Kodaira, S., Miura, S., Regalla, C., & Takahashi, N. (2013). High-resolution seismic imaging in the Japan Trench axis area off Miyagi, northeastern Japan. *Geophysical Research Letters*, *40*(9), 1713–1718. https://doi.org/10.1002/grl.50364

Nalbant, S., Steacy, S., Sieh, K., Natawidjaja, D., & McCloskey, J. (2005). Earthquake risk on the Sunda trench. *Nature*, *435*(7043), 756–757. https://doi.org/10.1038/nature435756a

Natawidjaja, D. H., Sieh, K., Chlieh, M., Galetzka, J., Suwargadi, B. W., Cheng, H., et al. (2006). Source parameters of the great Sumatran megathrust earthquakes of 1797 and 1833 inferred from coral microatolls. *Journal of Geophysical Research*, *111*(B6), B06403. https://doi.org/10.1029/2005JB004025

Newman, A. V., Hayes, G., Wei, Y., & Convers, J. (2011). The 25 October 2010 Mentawai tsunami earthquake, from real-time discriminants, finite-fault rupture, and tsunami excitation. *Geophysical Research Letters*, *38*(5), L05302. https://doi.org/10.1029/2010GL046498

Noda, H., Lapusta, N., & Kanamori, H. (2013). Comparison of average stress drop measures for ruptures with heterogeneous stress change and implications for earthquake physics. *Geophysical Journal International*, *193*(3), 1691–1712. https://doi.org/10.1093/gji/ggt074

Okuma, Y., Noda, A., Koge, H., Yamada, Y., Yamaguchi, A., & Ashi, Y. (2022). Surface friction of subducting seamounts influences deformation of the accretionary wedge. *Tectonophysics*, *845*, 229644. https://doi.org/10.1016/j.tecto.2022.229644

Park, J. O., Tsuru, T., Kodaira, S., Cummins, P. R., & Kaneda, Y. (2002). Splay fault branching along the Nankai subduction zone. *Science*, *297*(5584), 1157–1160. https://doi.org/10.1126/science.1074111

Philibosian, B., Sieh, K., Avouac, J. P., Natawidjaja, D. H., Chiang, H. W., Wu, C. C., et al. (2014). Rupture and variable coupling behavior of the Mentawai segment of the Sunda megathrust during the supercycle culmination of 1797 to 1833. *Journal of Geophysical Research: Solid Earth*, *119*(9), 7258–7287. https://doi.org/10.1002/2014JB011200

Philibosian, B., Sieh, K., Avouac, J. P., Natawidjaja, D. H., Chiang, H. W., Wu, C. C., et al. (2017). Earthquake supercycles on the Mentawai segment of the Sunda megathrust in the seventeenth century and earlier. *Journal of Geophysical Research: Solid Earth*, *122*(1), 642–676. https://doi.org/10.1002/2016JB013560

Philibosian, B., Sieh, K., Natawidjaja, D. H., Chiang, H., Shen, C., Suwargadi, B. W., et al. (2012). An ancient shallow slip event on the Mentawai segment of the Sunda megathrust, Sumatra. *Journal of Geophysical Research*, *117*(B5), B05401. https://doi.org/10.1029/02011JB009075

Pickering, K. T., Pouderoux, H., McNeill, L. C., Backman, J., Chemale, F., Kutterolf, S., et al. (2020). Sedimentology, stratigraphy and architecture of the Nicobar Fan (Bengal–Nicobar Fan System), Indian Ocean: Results from international ocean discovery program expedition 362. *Sedimentology*, *67*(5), 2248–2281. https://doi.org/10.1111/sed.12701

Prawirodirdjo, L., McCaffrey, R., Chadwell, C. D., Bock, Y., & Subarya, C. (2010). Geodetic observations of an earthquake cycle at the Sumatra subduction zone: Role of interseismic strain segmentation. *Journal of Geophysical Research*, *115*(B3), B03414. https://doi.org/10.1029/2008JB006139

Qin, Y. (2024). Sumatra Megatera box1 seismic time migration profiles [Dataset]. *Zenodo*. https://doi.org/10.5281/zenodo.10477365

Qin, Y., Nakamura, Y., Kodaira, S., & Fujie, G. (2022). Seismic imaging of subsurface structural variations along the Japan trench south of the 2011 Tohoku earthquake rupture zone. *Earth and Planetary Science Letters*, *594*, 117707. https://doi.org/10.1016/j.epsl.2022.117707

Qin, Y., & Singh, S. C. (2017). Detailed seismic velocity of the incoming subducting sediments in the 2004 great Sumatra earthquake rupture zone from full waveform inversion of long offset seismic data. *Geophysical Research Letters*, *44*(7), 3090–3099. https://doi.org/10.1002/2016GL072175

Qin, Y., & Singh, S. C. (2018). Insight into frontal seismogenic zone in the Mentawai locked region from seismic full waveform inversion of ultralong offset streamer data. *Geochemistry, Geophysics, Geosystems*, *19*(11), 4342–4365. https://doi.org/10.1029/2018GC007787

Repository, R. (2015). Cruise FK150523 on RV Falkor [Dataset]. *Rolling Deck to Repository (R2R) Program*. https://doi.org/10.7284/90158

Ruh, J. B., Sallarès, V., Ranero, C. R., & Gerya, T. (2016). Crustal deformation dynamics and stress evolution during seamount subduction: High-resolution 3-D numerical modeling. *Journal of Geophysical Research: Solid Earth*, *121*(9), 6880–6902. https://doi.org/10.1002/2016JB013250

Saffer, D. M., & Bekins, B. A. (2002). Hydrologic controls on the morphology and mechanics of accretionary wedges. *Geology*, *30*(3), 271–274. https://doi.org/10.1130/0091-7613(2002)030<0271:hcotma>2.0.co;2

Sak, P. B., Fisher, D. M., Gardner, T. W., Marshall, J. S., & LaFemina, P. C. (2009). Rough crust subduction, forearc kinematics, and Quaternary uplift rates, Costa Rican segment of the Middle American Trench. *GSA Bulletin*, *121*(7–8), 992–1012. https://doi.org/10.1130/B26237.1

Satake, K., Nishimura, Y., Putra, P. S., Gusman, A. R., Sunendar, H., Fujii, Y., et al. (2013). Tsunami source of the 2010 Mentawai, Indonesia earthquake inferred from tsunami field survey and waveform modeling. *Pure and Applied Geophysics*, *170*(9–10), 1567–1582. https://doi.org/10.1007/s00024-012-0536-y

Scholtès, L., & Donzé, F.-V. (2013). A DEM model for soft and hard rocks: Role of grain interlocking on strength. *Journal of the Mechanics and Physics of Solids*, *61*(2), 352–369. https://doi.org/10.1016/j.jmps.2012.10.005

Seyler, C. E., Kirkpatrick, J. D., Savage, H. M., Hirose, T., & Faulkner, D. R. (2020). Rupture to the trench? Frictional properties and fracture energy of incoming sediments at the Cascadia subduction zone. *Earth and Planetary Science Letters*, *546*, 116413. https://doi.org/10.1016/j.epsl.2020.116413

Sieh, K., Natawidjaja, D. H., Meltzner, A. J., Shen, C. C., Cheng, H., Li, K. S., et al. (2008). Earthquake supercycles inferred from sea-level changes recorded in the corals of West Sumatra. *Science*, *322*(5908), 1674–1678. https://doi.org/10.1126/science.1163589

Silver, E. A., Ellis, M. J., Breen, N. A., & Shipley, T. H. (1985). Comments on the growth of accretionary wedge. *Geology*, *13*(1), 6–9. https://doi.org/10.1130/0091-7613(1985)13<6:cotgoa>2.0.co;2

Singh, S. C., Carton, H., Tapponnier, P., Hananto, N. D., Chauhan, A. P. S., Hartoyo, D., et al. (2008). Seismic evidence for broken oceanic crust in the 2004 Sumatra earthquake epicentral region. *Nature Geoscience*, *1*(11), 777–781. https://doi.org/10.1038/ngeo336

Singh, S. C., Hananto, N., Mukti, M., Permana, H., Djajadihardja, Y., & Harjono, H. (2011). Seismic images of the megathrust rupture during the 25th October 2010 Pagai earthquake, SW Sumatra: Frontal rupture and large tsunami. *Geophysical Research Letters*, *38*(16), L16313. https://doi.org/10.1029/2011gl048935

Smith, G. L., McNeill, L. C., Wang, K., He, J., & Henstock, T. J. (2013). Thermal structure and megathrust seismogenic potential of the Makran subduction zone. *Geophysical Research Letters*, *40*(8), 1528–1533. https://doi.org/10.1002/grl.50374

Stevens, D. E., Henstock, T. J., & McNeill, L. C. (2021). Evolution of the thermal and dehydration state of sediments entering the North Sumatra subduction zone. *Geochemistry, Geophysics, Geosystems*, *22*(4), e2020GC009306. https://doi.org/10.1029/2020GC009306

Suppe, J. (1983). Geometry and kinematics of fault-bend folding. *American Journal of Science*, *283*(7), 684–721. https://doi.org/10.2475/ajs.283.7.684

Tsuji, T., Ashi, J., Strasser, M., & Kimura, G. (2015). Identification of the static backstop and its influence on the evolution of the accretionary prism in the Nankai Trough. *Earth and Planetary Science Letters*, *431*, 15–25. https://doi.org/10.1016/j.epsl.2015.09.011

von der Borch, C. C., Sclater, J. G., Gartner, S., Hekinian, J. R., Johnson, D. A., McGowran, B., et al. (2007). DSDP site 211. https://doi.org/10.2973/dsdp.proc.22.102.1974

Wang, K., & Hu, Y. (2006). Accretionary prisms in subduction earthquake cycles: The theory of dynamic Coulomb wedge. *Journal of Geophysical Research*, *111*(B6), B06410. https://doi.org/10.1029/2005JB004094

Widiwijayanti, C., Déverchère, J., Louat, R., Sébrier, M., Harjono, H., Diament, M., & Hidayat, D. (1996). Aftershock sequence of the 1994, M_w 6.8, Liwa earthquake (Indonesia): Seismic rupture process in a volcanic arc. *Geophysical Research Letters*, *23*(21), 3051–3054. https://doi.org/10.1029/96gl02048

Xia, Y., Kopp, H., Klaeschen, D., Geersen, J., Ma, B., & Schnabel, M. (2023). Seamount and ridge subduction at the Java margin, Indonesia: Effects on structural geology and seismogenesis. *Journal of Geophysical Research: Solid Earth*, *128*(9), e2022JB026272. https://doi.org/10.1029/2022JB026272

Yue, H., Lay, T., Rivera, L., Bai, Y. F., Yamazaki, Y., Cheung, K. F., et al. (2014). Rupture process of the 2010 M_w 7.8 Mentawai tsunami earthquake from joint inversion of near-field hr-GPS and teleseismic body wave recordings constrained by tsunami observations. *Journal of Geophysical Research: Solid Earth*, *119*(7), 5574–5593. https://doi.org/10.1002/2014JB011082